

Smart Manufacturing Approach for Efficient Operation of Industrial Steam-Methane Reformers

Ankur Kumar,[†] Michael Baldea,[†] Thomas F. Edgar,^{*,†} and Ofodike A. Ezekoye[‡]

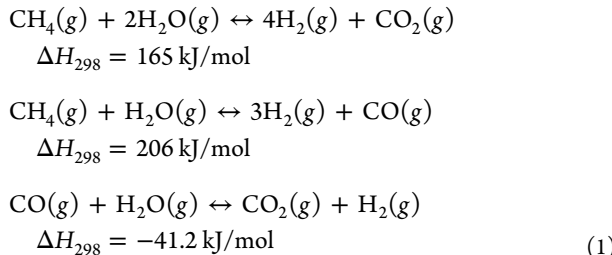
[†] McKetta Department of Chemical Engineering and [‡] Department of Mechanical Engineering, The University of Texas at Austin, Austin, Texas 78712, United States

S Supporting Information

ABSTRACT: Steam methane reforming is a mature and complex process extensively used worldwide for hydrogen production from methane. The process takes place in a steam methane reformer (SMR), with the endothermic reforming reactions being carried out in catalyst-filled tubes placed in a gas-fired furnace. The SMR is an energy-intensive process unit, and maximizing energy efficiency is of primary interest. However, the high-temperature conditions and large physical scale of the process (hundreds of tubes and burners) pose several operational challenges related to distributed sensing, actuation, and feedback control. Various efforts have been reported on optimization of furnace operation using rigorous computational fluid dynamics (CFD)-based models but, being computationally intensive, these models are unsuitable for real-time optimization. In this paper, we present an integrated framework that relies on the use of advanced temperature sensors, soft sensors, and reduced-order and rigorous SMR CFD models for distributed-parameter control of a hydrogen production test bed. We show a validation of our strategy through a case study on a representative SMR model. Furthermore, we describe the implementation of these methodologies in a readily deployable smart-manufacturing computational infrastructure.

INTRODUCTION

Steam reforming is a key step in the generation of syngas for the production of hydrogen, methanol, and ammonia. The reaction sequence includes endothermic reforming and the exothermic water–gas shift (see eq 1).



In industrial systems, these reactions take place inside catalyst-filled tubes that are placed in a gas-fired furnace.

Figure 1 shows a typical hydrogen plant where syngas from steam-methane reformer (SMR) goes through a shift reactor, followed by product (H_2) separation via pressure swing adsorption (PSA). In this process cycle, the SMR is the largest and most energy-intensive unit. With advances in process design and integration techniques, the scale of the process has become larger, with the production capacity of modern hydrogen production plants being greater than 100 MMSCFD of H_2 .¹

The energy for the reforming reactions is provided by combustion of a mixture of fresh natural gas feed and carbon monoxide-rich recycle from PSA beds. Figure 2 shows a schematic of a general top-fired SMR, wherein the burners and tubes are arranged in alternating rows. Hot flue gases exit the furnace along the extraction tunnels at the bottom and are used to preheat the incoming process gas.

In the hydrogen production cycle, the SMR is a critical unit and its efficiency contributes significantly to defining the productivity (energy consumed per unit H_2 produced) of the entire plant. In turn, SMR efficiency is dependent on the spatial temperature distribution inside the furnace (see Figure 3, presented later in this work). If the spatial temperature distribution is made more uniform, greater thermal efficiency can be obtained. We explain this aspect in detail in the next section. Depending on how well the furnace is operated, the nonuniformity in the tube-wall temperature (TWT), which is defined as the difference between the maximum and minimum TWT values at a fixed height for all the tubes, could vary by 30–110 K.² Various efforts have been made to understand the impact of design (burner design, etc.) and operating parameters (air/fuel distribution among different burners, etc.) on this temperature distribution. In order to adequately resolve the spatial temperature variation, the coupled heat transfer between the two distinct flow regions in a SMR (inside and outside the tubes) must be accurately modeled. The first attempts at coupled furnace-tube modeling include the work of McGreavy and Newmann.³ Since then, several researchers^{4–9} have studied various aspects of a top-fired/side-fired SMR. Most of these works^{1,4,6,8,9} do not distinguish between different tubes and lump them together for the purpose of TWT profile calculation. Plehiers and Froment⁷ treated each tube separately in a side-fired SMR and predicted a difference of 4–5 K between TWT values at a fixed height for uniform fuel flow

Special Issue: Scott Fogler Festschrift

Received: October 15, 2014

Revised: December 13, 2014

Accepted: December 16, 2014

Published: December 16, 2014

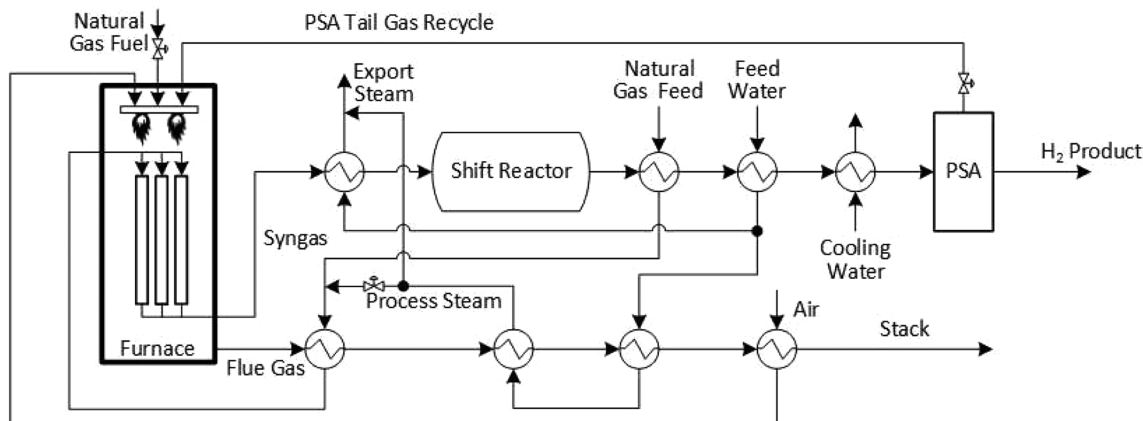


Figure 1. Schematic of a hydrogen production plant.³⁰

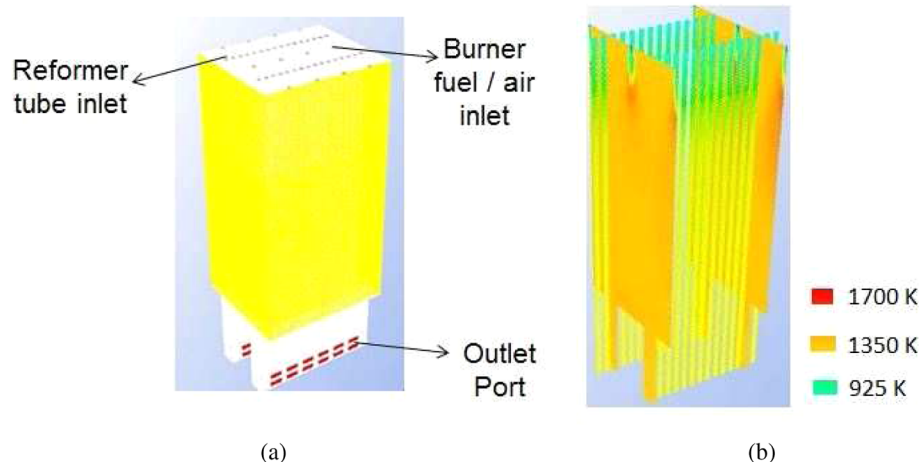


Figure 2. Schematic of (a) a typical top-fired steam-methane reformer (SMR) and (b) furnace (flue-gas and process-gas) temperature distribution.

distribution among burners. Dunn et al.⁵ took into account the different radiative environment experienced by tubes near the refractory walls and, therefore, treated the inner and outer row tubes differently. They carried out partial “furnace balancing” by minimizing the inner and outer row tube-wall temperature differences via adjustment of “burner profile” and reactant gas distribution. These works mainly use radiative heat-transfer zone models that ignore the impact of flue gas flow pattern, such as recirculation, which can have significant impact on the TWT.¹⁰ Another drawback of such simplified models is the neglect of transverse temperature variations of the furnace gas, leading to inaccurate tube temperature predictions. Oprins et al.¹¹ combined the zone method with a detailed computational fluid dynamics (CFD) model to resolve the realistic flow field in a coupled furnace-reactor system and showed that thermal efficiency can be improved by nonuniform heating. Using rigorous CFD models, Zheng et al.¹² have shown that the maldistribution of flue gas impacts the temperature distribution, leading to hot spots. Slavejov et al.² attempted to reduce temperature nonuniformity through heuristics-based manual fuel-flow adjustments.

To our knowledge, there has been no published work on industrial application of rigorous model-based real-time furnace operation optimization for the reduction of temperature nonuniformity. There are various aspects that make this difficult, primarily, the lack of continuous temperature measurements of all the tubes. In practice, thermocouples

(TCs) provide real-time temperature measurement. However, TCs are typically installed only on some of the tubes. These limited data are insufficient for a complete estimation of furnace temperature distribution. Moreover, rigorous SMR models have large computational times that inhibit their adoption for real-time optimization. Also, the spatial temperature distribution is dependent on various disturbances that affect the furnace, such as variations in ambient conditions, combustion air distribution, etc. This rules out the possibility of making (offline) a unique determination of optimal fuel distribution for all operating conditions. The optimal fuel distribution changes under the impact of disturbances and should therefore be recomputed regularly online.

In this study, we report the use of an array of infrared (IR) camera sensors, which produce a significant stream of data regarding the furnace temperature distribution, and a smart-manufacturing platform (SMP). While the IR cameras provide furnace-wide temperature measurements, SMP provides appropriate computational resources for determining the optimal furnace balancing strategy. This work comprises the first application of distributed-parameter control of SMRs.

In the next section, we explain the concept behind furnace balancing followed by a description of the SMP. Crucial aspects of furnace balancing are examined using a prototype SMR model. We then show how CFD and reduced-order models, and infrared (IR) camera data-based soft sensor are deployed on SMP for improved SMR operation. We conclude with

implementation of the proposed mechanism on the simplified SMR model to illustrate its performance.

FURNACE BALANCING

Theoretically, reforming reactions being net endothermic achieve higher methane conversion at higher temperature. However, the temperature at which the SMR furnace can be operated is limited by various factors, such as the creep limit of the reformer tube material. Generally, the design life of a reformer tube is 100 000 h, but its service life is extremely sensitive to the TWT. A 20 K increase in the TWT value over the design temperature decreases its life by one-half.¹ Any failure due to tube rupture entails significant economic costs due to plant shutdowns and production losses. The furnace is often operated below even this design value to keep TWT values at safe margin from the design temperature. Figure 3

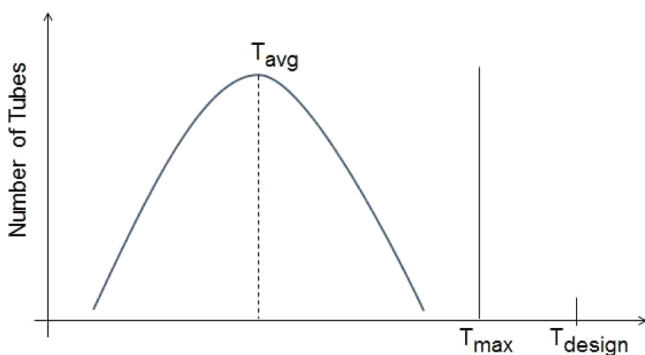


Figure 3. Distribution of tube-wall temperature (TWT) at a fixed height of all the tubes.

shows the typical TWT distribution in an SMR. The TWT nonuniformity is inherently a function of the flue gas pattern, which, in turn, is strongly dependent on fuel/air distribution.

While a few tubes operate close to maximum allowable temperature, many operate at much lower temperatures. Overall, the average temperature is much lower than the design temperature, leading to suboptimal syngas yield. Furthermore, a nonuniform furnace temperature leads to lower radiant box efficiency and thus energy loss. *Furnace balancing* refers to reducing this temperature nonuniformity, while keeping the average temperature the same, as shown in Figure 4a. This can, e.g., be achieved by partially closing the fuel valves of a few burners (assuming that all valves are 100% open initially) which lie in hotter regions of the furnace by

appropriate amounts. Since the total fuel input does not change, this results in redistribution of fuel from hotter regions to colder regions. To obtain the optimal fuel distribution, a rigorous model is required that can accurately predict the tube temperature profile as a function of fuel flow. This is described in later sections.

Although achieving a reduced temperature nonuniformity does have some advantages, in terms of longer tube life and reduced NO_x emissions, major benefits are derived from driving the average temperature to a greater value by increasing total fuel input, as shown in Figure 4b. This leads to greater process gas outlet temperature and, thus, greater H₂ production. Apart from higher H₂ production, greater flue gas temperature leads to higher production of export steam (see Figure 1). When this greater total enthalpy of the export steam product is taken into account, along with the higher H₂ yield, it leads to lower overall energy consumption per unit H₂ produced. Overall, it is estimated that 1% reduction in energy costs for a 100 MMSCFD plant can lead to a savings of \$600 000/yr.¹

SMART MANUFACTURING

In previous sections, we mentioned the need to have greater integration of process data and advanced high-fidelity models for a real-time decision support system. Enterprise-wide integration of data management and analysis tools is limited in small- and medium-scale enterprises, because of high investment cost. Smart manufacturing addresses this challenge through pervasive adoption of cost-effective infrastructure for integration of manufacturing intelligence in real time across an entire production line.¹³ This goal is being pursued by some industries by development of a platform that can lower the cost of the information technology (IT) infrastructure, sensing, modeling, and simulation deployment, resulting in higher energy productivity. The work presented in this paper is an initial proof-of-concept to demonstrate the feasibility of this objective. It is realized in the form of a cloud-based workflow environment with customizable templates for process data collection, processing, analysis, and output dissemination.¹⁴ The SM platform allows us to carry out high-performance distributed computing calculations on remote hardware resources with low network latency and high input/output bandwidth providing high parallelization scalability for computation intensive simulations such as CFD calculations. Employing multiple compute servers and storage units, the SM platform is capable of peak performance greater than 100 TFLOPS (tera floating-point operations per second) when fully

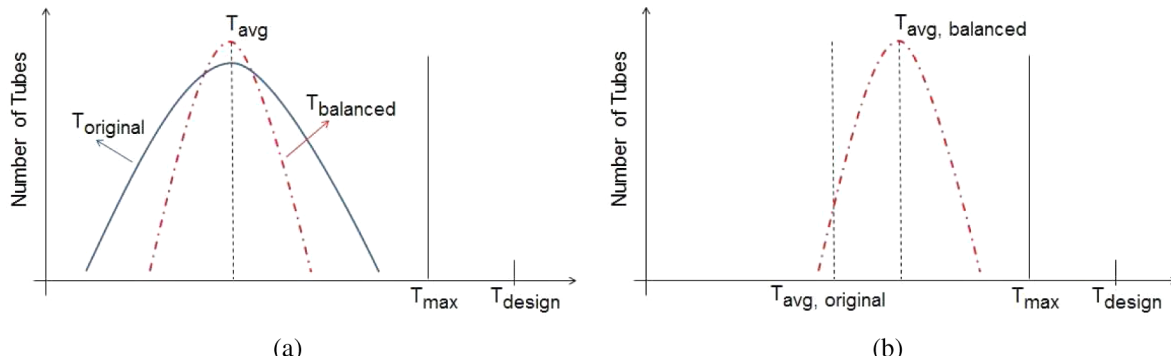


Figure 4. (a) Reduction in TWT nonuniformity. (b) Increase in average TWT.

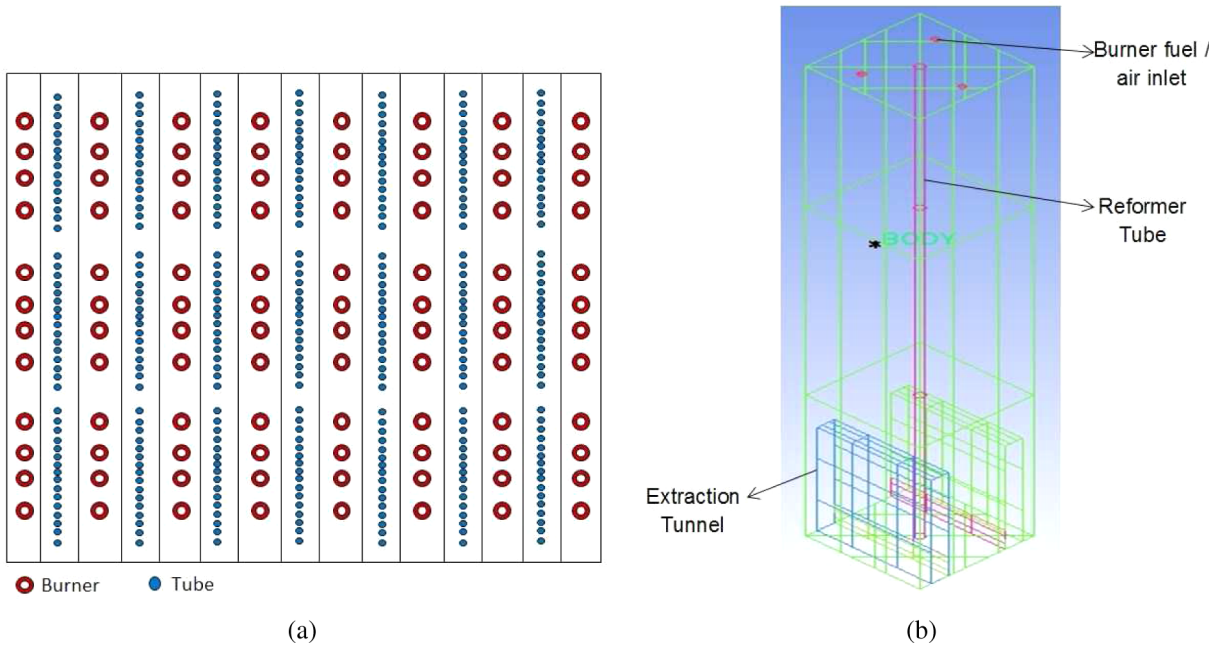


Figure 5. (a) Schematic of top-view of test-bed SMR.¹ (b) Small-scale SMR geometry (12.5 m × 2 m × 2 m).

Table 1. Reforming Kinetics^a

reaction	reaction rate
$\text{CH}_4(g) + \text{H}_2\text{O}(g) \leftrightarrow 3\text{H}_2(g) + \text{CO}(g)$	$r_1 = \frac{k_1}{p_{\text{H}_2}^{2.5}} \left(p_{\text{CH}_4} p_{\text{H}_2\text{O}} - \frac{p_{\text{H}_2}^3 p_{\text{CO}}}{K_1} \right) / \text{DEN}^2$
$\text{CO}(g) + \text{H}_2\text{O}(g) \leftrightarrow \text{CO}_2(g) + \text{H}_2(g)$	$r_2 = \frac{k_2}{p_{\text{H}_2}} \left(p_{\text{CO}} p_{\text{H}_2\text{O}} - \frac{p_{\text{H}_2} p_{\text{CO}_2}}{K_2} \right) / \text{DEN}^2$
$\text{CH}_4(g) + 2\text{H}_2\text{O}(g) \leftrightarrow 4\text{H}_2(g) + \text{CO}_2(g)$	$r_3 = \frac{k_3}{p_{\text{H}_2}^{3.5}} \left(p_{\text{CH}_4} p_{\text{H}_2\text{O}}^2 - \frac{p_{\text{H}_2}^4 p_{\text{CO}_2}}{K_3} \right) / \text{DEN}^2$

^aData taken from ref 22. DEN = 1 + $K_{\text{CO}} p_{\text{CO}} + K_{\text{H}_2} p_{\text{H}_2} + K_{\text{CH}_4} p_{\text{CH}_4} + K_{\text{H}_2\text{O}} p_{\text{H}_2\text{O}} / p_{\text{H}_2}$.

deployed. In the next few sections, we discuss the development of the CFD and reduced-order models that form the core of the data analysis component of the platform.

CFD-BASED SMR MODEL

The magnitude of the reduction in furnace temperature nonuniformity that is sought for the subsequent increase in average temperature is, relatively, much smaller, compared to the absolute temperature at which the furnace is operated. Thus, it becomes imperative to estimate the furnace temperature distribution with high accuracy. CFD provides a way for such rigorous analysis of complicated flue gas flow in the heterogeneous distributed parameter furnace system while incorporating detailed models for turbulence, combustion, radiation, and reforming reactions. Oprins and Heynderickx,¹⁵ Stefanidis et al.,¹⁶ and Habibi et al.¹⁷ have investigated the effects of different grid structures, combustion mechanisms, and radiation models, respectively, on furnace and tube walls, and flue gas temperature profiles in steam cracking furnaces. The test bed used in this study has 8 rows of 12 burners each and 7 tube rows with 48 tubes in each row, as shown in Figure 5a. The simulation time of high-resolution CFD models of such large-scale systems can exceed several hours, even on supercomputing clusters. Consequently, it becomes crucial to

identify the avenues for reduction in simulation time without substantially compromising on the model accuracy. In this spirit, CFD models with smaller subset of burners and tubes are studied first, followed by gradual increments in the model's complexity. Figure 5b shows a prototype SMR with one reformer tube and three burners.

The meshed domain, created using ICEMcfd,¹⁸ comprises 1.8 million cells. The model was simulated in Fluent,¹⁸ which uses finite-volume method to solve the governing equations. The flow inside the tube is resolved using the "reacting channel" model¹⁹ provided by Fluent, and is approximated as a plug flow (radial variations are ignored). This is suitable for geometries such as that of an SMR, where the reacting fluid that resides inside long and relatively thin tubes exchange heat with the flue gas outside the tubes. Tables S1 and S2 in the Supporting Information summarize the set of equations solved for the tube side process gas and the furnace side flue gas, respectively. Additional parameter values employed in the CFD model are included in Table S3 in the Supporting Information.

Heat transfer to the tube is mostly dominated by radiation from the flame, flue gas, and the refractory walls and has been modeled using the P1 radiation model.²⁰ Habibi et al.¹⁷ have shown that accuracy of the P1 model is similar to that of discrete ordinates model, and its computational overhead is

Table 2. Derived Standard Arrhenius Kinetics Form for Reforming Reactions^a

$k_r = A_r T^{\beta_r} \exp\left(-\frac{E_r}{RT}\right)$				
		A_r	β_r	E_r
$\text{CH}_4(g) + \text{H}_2\text{O}(g) \leftrightarrow 3\text{H}_2(g) + \text{CO}(g)$	$r_1 = \frac{k_1}{[C_{\text{H}_2}]^{2.5}} [C_{\text{CH}_4}] [C_{\text{H}_2\text{O}}]$	3.66×10^{14}	-2.05	2.401×10^8
	$r_{-1} = k_{-1} [C_{\text{CO}}] [C_{\text{H}_2}]^{0.5}$	5.38	-0.05	3.4×10^7
$\text{CO}(g) + \text{H}_2\text{O}(g) \leftrightarrow \text{CO}_2(g) + \text{H}_2(g)$	$r_2 = \frac{k_2}{[C_{\text{H}_2}]^{1.5}} [C_{\text{CO}}] [C_{\text{H}_2\text{O}}]$	4.06×10^4	-0.55	6.7×10^7
	$r_{-2} = k_{-2} [C_{\text{CO}_2}]$	2.17×10^6	-0.55	1.08×10^8
$\text{CH}_4(g) + 2\text{H}_2\text{O}(g) \leftrightarrow 4\text{H}_2(g) + \text{CO}_2(g)$	$r_3 = \frac{k_3}{[C_{\text{H}_2}]^{3.5}} [C_{\text{CH}_4}] [C_{\text{H}_2\text{O}}]^2$	3×10^{14}	-2.05	2.44×10^8
	$r_{-3} = k_{-3} [C_{\text{CO}_2}] [C_{\text{H}_2}]^{0.5}$	113	-0.05	7.9×10^7

^aUnits for parameters given in table: r , kmol/(m³ s); E_r , J/kmol; β_r , dimensionless; T , K; and $[C]$, kmol/m³.

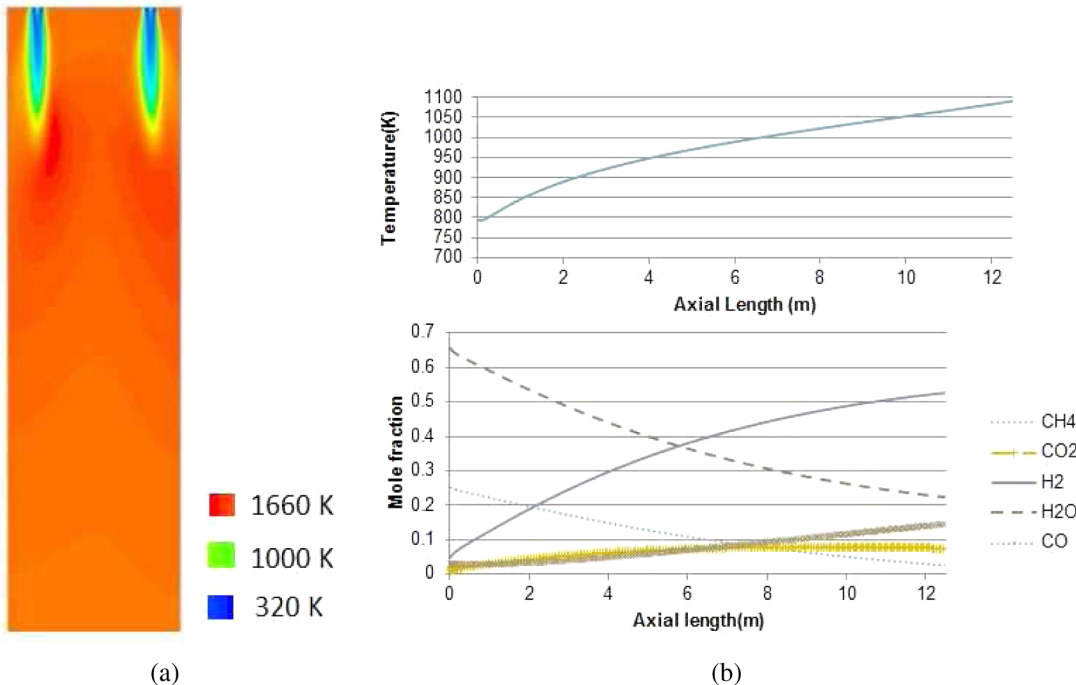


Figure 6. Results for the prototype SMR: (a) temperature distribution along a vertical plane through burners and (b) temperature and composition profile inside the reformer tube.

much lower. To adequately resolve heat transfer at the walls, the enhanced wall treatment function^{19,21} is used, which is recommended because it relaxes the requirement of a very fine mesh near the walls without compromising solution accuracy. Pressure outlet boundary conditions are imposed at the tube and furnace outlets. For reforming reactions, the kinetic formulation derived by Xu and Froment,²² as shown in Table 1, is widely used. However, such kinetic formulations are usually implemented using custom-defined routines, which generally tend to slow the computation, apart from causing convergence issues. Moreover, the kinetic parameters change over time, because of the natural degradation of catalyst activity and poisoning from carbon deposition over the catalyst surfaces. Thus, these parameters must be regularly updated.

To circumvent the use of custom routines, and facilitate convenient updates, an alternative kinetic formulation compatible with Fluent's built-in reaction scheme is used in this work, the parameters of which were derived through regression against predictions from Xu and Froment's kinetic form. The values are shown in Table 2. An overall effectiveness factor is used to account for diffusion limitations in the catalyst.

The process gas temperature and composition profile obtained after implementation of this alternative kinetics is shown in Figure 6. A second-order upwind scheme is employed for discretization of the governing equations. A pseudo-transient solver is used, which, along with appropriate under-relaxation factors, aids in smooth convergence. As expected, the temperature in the furnace is highest at the tip of the flames,

Table 3. Fuel Distribution Scheme for the CFD Simulations of the Prototype SMR^a

flow rate (kg/h)	set-1			set-2		
	case 1	case 2	case 3	case 1	case 2	case 3
burner 1 (f_1, γ_1)	82.8, (1/3)	99.4, 0.4	99.4, 0.4	90, (1/3)	108, 0.4	108, 0.4
burner 2 (f_2, γ_2)	82.8, (1/3)	74.5, 0.3	77.8, 0.313	90, (1/3)	81, 0.3	84.6, 0.313
burner 3 (f_3, γ_3)	82.8, (1/3)	74.5, 0.3	71.2, 0.287	90, (1/3)	81, 0.3	77.4, 0.287

$$f_{\text{total}} = f_1 + f_2 + f_3$$

$$f_{\text{total}} = 248.4$$

$$f_{\text{total}} = 270$$

^aParameter f denotes the flow rate (in kg/h); γ represents the fuel distribution ratio. γ_i (case k , set-1) := f_i (case k , set-1)/ f_{total} (set-1) = γ_i (case k , set-2).

whereas inside the tube, the temperature gradually increases from 800 K at the inlet to ~1100 K at the outlet. The average heat flux into the reformer tube is 60 kW/m². One observation is that the simplified kinetics lead to output profiles that lie close to the industrially observed values.⁵ We use this model to study the impact of fuel maldistribution on flue gas temperature distribution. Since the TWT is correlated to the surrounding flue gas temperature, one can understand various crucial aspects of furnace balancing from the observed patterns in flue gas temperature distribution and extend the inferred insights to real-plant balancing.

Aspects of Furnace Balancing. To understand the impact of fuel distribution on furnace-temperature field, nonuniformities in the fuel flow through the burners were imposed in the prototype system by increasing the heat duty of one of the burners (burner 1 in Table 3) by 20%, and recording the flue gas temperature distribution at axial locations of 6 and 3.5 m from the top. The total fuel input is kept the same by redistributing the fuel among the three burners appropriately. Next, the total fuel input was increased by ~10% and the same nonuniformities as those previously noted were imposed. We will refer to the set of simulations with the original total heat duty as set-1, whereas the latter set of simulations with higher heat-duty will be referenced as set-2. Table 3 shows the simulation scheme where case 1 (for each set) refers to simulation with uniform fuel inputs to the three burners. Cases 2 and 3 refer to the simulations with nonuniformities where either one burner (case 2) or all three burners (case 3) have different fuel inputs. The nonuniformity of corresponding cases in the two sets is kept identical by imposing the same fuel distribution ratio (ratio of individual fuel flow through a burner to total fuel flow). For example, the distribution ratios ($\gamma_1, \gamma_2, \gamma_3$) for case 3 in both sets are 0.4, 0.313, and 0.287, respectively. The range (maximum TWT – average TWT) and the standard deviation (σ) of the temperature distribution are used to quantify its nonuniformity. Table 4 shows the observed data.

Many points are worth discussing here. As expected, within a given set, the mean temperature does not change significantly, since the total fuel input remains the same. The temperature distribution becomes more nonuniform (higher deviation (σ) and range) when subjected to nonuniform fuel flow. Although, for our case study, a uniform fuel distribution leads to a “balanced” furnace, it may or may not be the optimal scenario in a real plant, where the furnace might be “unbalanced”, even with a uniform fuel distribution. As mentioned earlier, factors such as air distribution, ambient conditions, process feed distribution, etc. affect the furnace temperature field. A very significant result is the observation that the temperature nonuniformity is not a strong function of net heat duty (or total fuel input). This can be inferred by comparing the distribution statistics between the two simulation sets for

Table 4. Flue-Gas Temperature Distribution Statistics^a for the Prototype SMR (a) at a Distance of 6 m from the Top and (b) at a Distance of 3.5 m from the Top

	set-1			set-2 ^b		
	case 1	case 2	case 3	case 1	case 2	case 3
(a) 6 m from the Top						
mean	1501	1502	1502	1573	1575	1575
max – mean	10	28	28	12	29	29
2σ	10.8	19.9	20.4	11.8	19.6	20.2
(b) 3.5 m from the Top						
mean	1522	1528	1529	1598	1604	1605
max – mean	27.8	99.5	99	33	109	109
2σ	21.4	69.2	70	26	74	74.8

^aAll values given in units of Kelvin (K). ^bEquivalent process gas outlet temperature increase in set-2 is ~29 K.

corresponding cases. While the mean temperatures increase upon increase of the heat duty, the deviations (σ) are similar. This observation has important implications. Referring back to our original objective of achieving higher energy productivity through higher mean tube temperature, as shown in Figure 4, we intended to increase the heat duty after “balancing” the furnace, under the assumption that, with reduced nonuniformity, the maximum tube temperature will not cross the upper threshold upon increasing the net heat duty. This assumption would have been invalidated had the nonuniformity been strongly dependent on the total fuel input, and would have implied “rebalancing”, along with probable damage to the tubes. Also, although the temperature distribution changes along the length of the furnace, the nonuniformity reduction pattern/behavior seems to be relatively independent of the axial location, primarily because of the underlying correlation among the corresponding temperatures at different heights. The importance of such independence can be realized in connection with the formulation of an appropriate minimization objective in an optimization scheme for the reduction of temperature nonuniformity. Such an “equivalence” among the temperature distributions at different heights implies a favorable lower-dimensional optimization problem. It should be noted that this “equivalence” does not imply the lack of importance of complete temperature measurements along the entire length of the tubes, such as that obtained through IR sensors. Knowledge of the complete temperature profile becomes crucial when driving up the process gas outlet temperature, as well as during reconstruction of unmeasured temperature values (explained later). The graphical depiction of the temperature field data at 6 m from the top is presented in Figure 7, as a realization of the concept shown in Figure 4.

Unit-Cell Modeling. In Figure 5a, we showed the geometry/tube-burner layout of the SMR plant under study

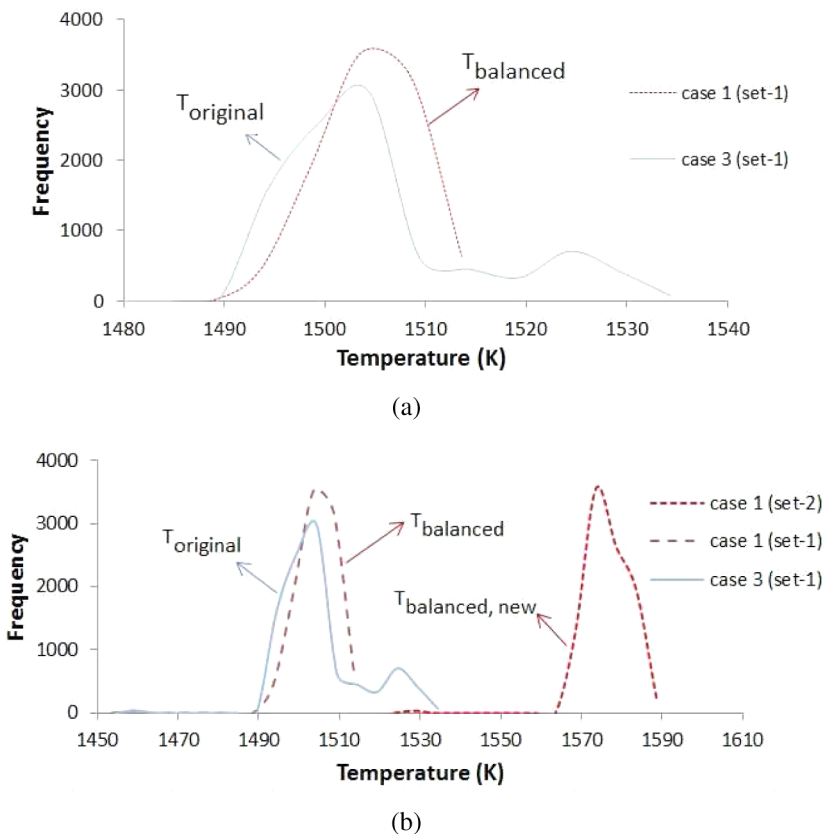


Figure 7. Realization of furnace balancing for the single-tube steam-methane reformer (SMR): (a) reduction of temperature nonuniformity and (b) increase of mean temperature (the equivalent process gas outlet temperature increase is ~ 29 K).

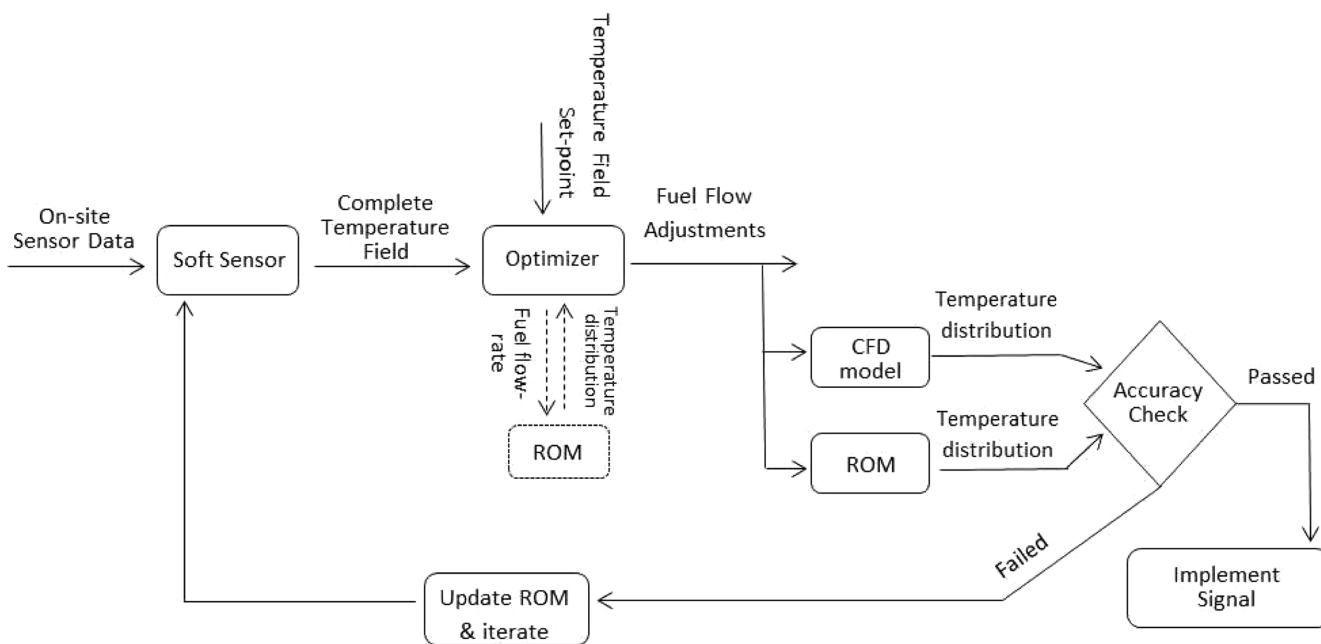


Figure 8. Overview of the algorithmic sequence for distributed-parameter control of the SMR.

in this work. A very natural extension of the single-tube SMR model before full-scale CFD modeling is a 32-tube and 12-burner subsection (the meshed domain shown in Figure 2a). We call this subsection a unit cell of the SMR. A unit cell, by definition, mirrors the overall behavior of a larger system at the local scale. While the behavior of the larger scale system can be

predicted quite accurately through appropriate combination of predictions from a suitable assortment of unit cells, the computational overhead is reduced substantially, because of unit cell modeling. The assertion is partly based on the clear grouping of tubes and burners, as seen in Figure 5a. The unit-cell CFD model comprises 5.8 million cells and has a steady-

state simulation time of a few hours on a high-performance computing cluster. The modeling strategy of the single-tube SMR model was replicated with a change of boundary conditions at the symmetrical lateral surfaces of the unit cell. The predicted temperature contour for the fluid region inside the tubes and along two vertical planes that pass through the burners can be seen in Figure 2b.

The purpose behind introducing the unit cell here is to emphasize the large computational requirements, even after the adoption of unit-cell-based modeling. This motivates even greater reduction of model order to enable the use of these CFD models online. This is the subject of our discussion in the next section.

REAL-TIME DEPLOYMENT

Industrial SMR plants generally employ plantwide advanced control schemes, such as model predictive control or cascade control, for regulating the reformer product temperature, but the performance of the furnace itself is not monitored/regulated in real time. General practice involves making manual TWT measurements using hand-held pyrometers, followed by heuristics-based adjustments in fuel flow. Understandably, this is highly inefficient. The lack of continuous furnace-wide temperature measurements, combined with unavailability of a sufficiently accurate model that runs in real-time, results in suboptimal furnace operation. To tackle the first issue, several IR cameras were installed around a SMR furnace at a hydrogen production facility.

While the CFD model does provide accurate predictions in reasonable time when run using supercomputing facilities on a steam methane (SM) platform, it is still prohibitive to use the CFD model within an optimization scheme designed to improve furnace operation. A common practice instead is to use reduced-order models (ROMs)²³ that show similar input–output relationship but have much lower computational time. A potential drawback of this strategy is lower prediction accuracy at input points that are away from the design input space utilized while developing the ROM. Adaptive modeling overcomes this drawback by updating the model upon availability of new measurements. Figure 8 shows a schematic of implementation of combined adaptive ROM and CFD that enables real-time computation of optimal fuel distribution based on temperature data.

A soft-sensor module takes in the measurements including the IR data from the plant site and reconstructs the complete temperature field (a few tubes lie in the blind zone of the cameras, i.e., they do not lie in the cameras' field of view). Next, the optimizer module uses the ROM to find the optimal fuel flow adjustments that minimize the TWT nonuniformity. However, before the suggested adjustments are implemented, the proposed adjustments are first vetted against CFD predictions. If temperature predictions from CFD and ROM are within a specified threshold, then the computed flow adjustments are communicated to the plant operators. Alternatively, the new set of data from the CFD calculations are used to update the ROM, and the optimal flow is recomputed.

Before we present a case study using the single-tube SMR model, where we implement the scheme shown in Figure 8, the general mathematical framework of the methodologies employed for reduced-order modeling and soft sensing is presented in the following subsections.

Reduced-Order Modeling. The CFD model contains millions of state variables, arising from discretization of the spatial domain, and, therefore, is high-dimensional. However, for a furnace system, these dimensions are highly correlated and can usually be projected onto a lower-dimensional subspace without a substantial loss of accuracy. Proper orthogonal decomposition (POD)²⁴ has been used successfully for such projection-based order reduction of nonlinear distributed parameter systems.^{25,26} Following the exposition by Lang et al.,²⁶ we briefly present the data-driven framework for steady-state POD modeling.

POD computes a set of orthogonal basis functions $\phi_1, \phi_2, \dots, \phi_k \in \mathfrak{R}^N$, such that the projection of the N -dimensional variable of interest (discretized TWT values here) on the subspace spanned by these k basis functions is optimal for any k -dimensional subspace.

$$T \approx \sum_{j=1}^k a_j \phi_j \quad k \ll N \quad (2)$$

where $T \in \mathfrak{R}^N$ are TWT values, and $a = [a_1, a_2, \dots, a_k]^T \in \mathfrak{R}^k$ are POD coefficients that are functions of f , the input fuel-flow rates. The value of k is usually chosen such that the loss of accuracy upon projection is $<0.01\%$. The basis functions can be computed through singular value decomposition (SVD) of the data matrix $M \in \mathfrak{R}^{N \times p}$, which is a collection of p N -dimensional temperature (T) vectors. These temperature data come from either physical experiments or simulations of a high-fidelity model such as a CFD model. Thus, every column in the data matrix M is an instance of " T " vector obtained from one of the p experiments or simulations. Each of these p experiments/simulations corresponds to a different input fuel distribution. The next step involves determination of a functional relationship between coefficient vector a and model inputs, i.e., $F_j(f) : f \rightarrow a_j$, where F is the required mapping. Thus, using eq 3, the temperatures can be predicted as a function of input variables.

$$T \approx \sum_{j=1}^k F_j(f) \phi_j \quad (3)$$

The accuracy of any data-driven ROM predictions at a test point is dependent on the distance of the point from the design input space that was considered during the generation of the data matrix. In the case of poor prediction, the model can be efficiently updated using adaptive POD techniques (e.g., see the work of Varshney et al.²⁷), where the basis functions are recomputed efficiently in light of availability of new measurements.

Soft Sensing. By definition, a soft sensor provides software-based measurements inferred from other measurements versus direct measurements of process variables that are difficult or impossible to measure. In our scheme of analysis, the soft-sensor block in Figure 8 estimates the temperature profile of tubes that fall in the "blind zone" of the cameras and thus could not be imaged. For soft sensing, we employ the missing point estimation algorithm,²⁸ as briefly presented below. Let \tilde{T} denote the vector of temperature values corresponding to discretized locations that are under measurement. Thus,

$$\tilde{T} = \tilde{I} \times T \quad (4a)$$

and, similarly,

$$\tilde{\phi} = \tilde{I} \times \phi \quad (4b)$$

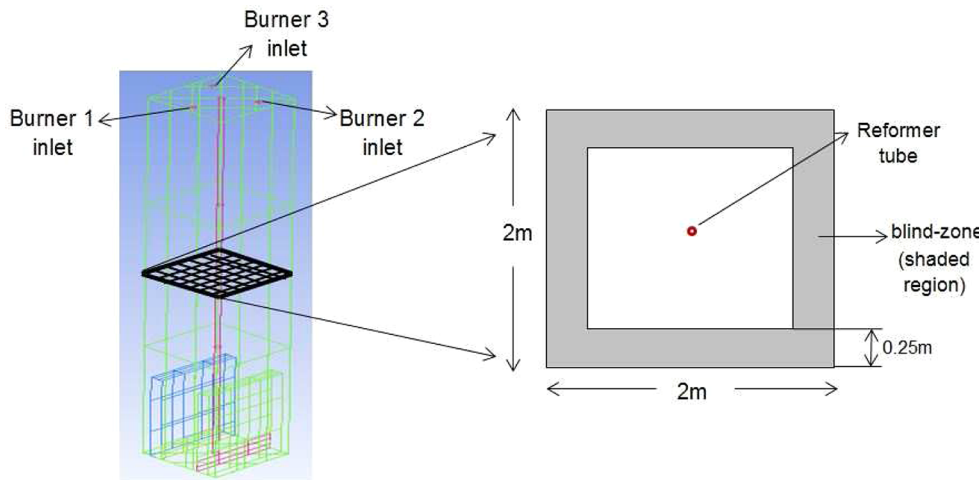


Figure 9. “Sensed” transverse cross-section plane at a height of 6 m from the top, and the blind zone of the temperature sensors. Temperature data (discretized) for only the concentric square region of side length 1.5 m (~57%) is assumed available.

where \tilde{T} is an appropriate mask matrix while T and ϕ are as defined in eq 2. Combining eqs 2 and 4 yields

$$\begin{aligned} \tilde{T} &\approx \sum_{j=1}^k \hat{a}_j \tilde{\phi}_j \\ &\Rightarrow \sum_{j=1}^k \hat{a}_j \langle \tilde{\phi}_j, \tilde{\phi}_i \rangle = \langle \tilde{T}, \tilde{\phi}_i \rangle \quad i = 1, \dots, k \\ &\Rightarrow M\hat{a} = c \end{aligned} \quad (5)$$

where

$$M_{ij} = \langle \tilde{\phi}_i, \tilde{\phi}_j \rangle \quad \text{and} \quad c_i = \langle \tilde{T}, \tilde{\phi}_i \rangle$$

Here, the construct $\langle \cdot \rangle$ is a vector dot product. M is not an identity matrix as unlike ϕ , $\tilde{\phi}$ are not orthonormal, and, in fact, are not even orthogonal. Equation 5 can be solved for \hat{a} to eventually give the complete temperature field: $T \approx \sum_{j=1}^k \hat{a}_j \phi_j$. While the total fuel flow is measured, the flows to individual burners are unknown. Using the POD coefficients determined in eq 5, these individual flows can be estimated through the following scheme:

$$\min_f \| \hat{a} - F(f) \| \quad (6)$$

subject to

$$\sum_j f_j = \text{fuel}_{\text{total}}$$

$$f \geq 0$$

where $\| \cdot \|$ is a vector 2-norm, f_j is the fuel-flow through the j th burner, and $F = [F_1, F_2, \dots, F_k]^T \in \mathfrak{R}^k$ is the mapping, as shown in eq 3. This formulation is computationally more efficient, compared to the minimization of $\| T - \sum_{j=1}^k F_j(f) \phi_j \|$, since the dimensionality of \hat{a} is much smaller than the dimensionality of T .

CASE STUDY ON THE SINGLE-TUBE SMR MODEL

In Figure 7a, we demonstrated that the fuel distribution can be modified so that it provides greater uniformity in the furnace temperature field. In Figure 8, we presented a control scheme

to enable real-time SMR optimization through furnace-balancing. In this case study, we drive the prototype single-tube SMR (Figure 5b) from an unbalanced state to a relatively balanced state. A discretized temperature distribution at 6 m from the top (Figure 9) is assumed as sensor input from an IR camera system to the control scheme. It is further assumed that a part of the cross section lies in the blind zone of the sensors, so a full temperature profile is not available. This is analogous to the TWT data from the IR cameras in case of the real plant.

Case 3 of set-1 (in Table 3), with the input fuel flow being $f = [99.4, 77.8, 71.2]^T$ kg/h, and, consequently high non-uniformity, are assumed to be the initial furnace conditions.

ROM. A POD-based ROM is generated for this SMR model. Here, $T \in \mathfrak{R}^N$, where $N = 9735$ and $f \in \mathfrak{R}^3$. T is a vector of the temperature values at grid points along the plane at a height of 6 m from the top. The training dataset is composed of temperature outputs from 27 CFD simulations, with input conditions designed using the Latin Hypercube Sampling (LHS) method.²⁹ Each input fuel-flow range is $50 \text{ kg/h} \leq f_j \leq 100 \text{ kg/h}$ ($j = 1, 2, 3$) in the LHS design. Three POD basis functions are able to capture 99.9% variance of the training dataset (i.e., $k = 3$), and a linear mapping from $f \xrightarrow{B} a$ (where $B \in \mathfrak{R}^{3 \times 4}$ is the matrix of coefficients of the linear mapping) gives sufficiently accurate predictions. Thus,

$$\begin{aligned} T &= \Psi a \\ &= \Psi B \bar{f} \end{aligned} \quad (7)$$

where

$$\Psi = [\phi_1, \phi_2, \phi_3]$$

and

$$\bar{f} = [1, f^T]^T$$

Since the individual flow rates are unknown, and changes in these fuel flows (rather than absolute flows) are the desired control outputs, an alternative deviation form of eq 7 can be written:

$$\Delta T = G \Delta f \quad (8)$$

In eq 8, G is simply the first three columns of the matrix ΨB . This deviation form is used in the optimizer module for this case study.

Soft Sensor. Here, $\tilde{T} \in \Re^{5617}$. The temperatures in the blind zone and the individual fuel flow rates are estimated using eqs 5 and 6.

Optimizer. This module uses the estimated complete temperature distribution and fuel flow rates to compute optimal fuel flow adjustments per the following scheme:

$$\min_{\Delta f} \sigma(T) \quad (9)$$

subject to

$$T = T_o + G\Delta f$$

$$\sum_{i=1}^3 \Delta f_i = 0$$

$$\Delta f_i \geq -f_{i,o} \quad i = 1, 2, 3$$

where $\sigma(T)$ is the standard deviation of T , Δf is the required fuel-flow adjustment, and T_o and $f_{i,o}$ are the estimated initial complete temperature field and fuel-flow rates, respectively.

The results are shown in Table 5. No model updates were carried out, since the solution computed in the very first

Table 5. Results from “Furnace Balancing” Attempted through the Proposed Control Scheme

	initial condition	estimated condition	computed optimal solution
f_1 (kg/h)	99.4	97	85.5
f_2 (kg/h)	77.8	78.8	80.4
f_3 (kg/h)	71.2	72.6	82.5
2σ (K)	20	20	10.8
range (K)	28	26.6	11

iteration gave satisfactory results. The computational overhead of the non-CFD calculations is a few seconds and, thus, the run time is dominated by CFD calculations, which were ~ 4 h on a standard desktop system, primarily due to the single CFD simulation that was carried out to check the accuracy of the computed solution. The optimal solution is close to the uniform flow conditions depicted by case 1 of set-1 in Table 3, which corresponds to a uniform flow of 82.8 kg/h; therefore, the change in temperature distribution from the unbalanced state to the balanced state is similar to that shown in Figure 7a. The distribution statistics for the “optimal solution”, as shown in Table 5, are based on CFD outputs with the “optimal flows”.

Color contours of the flue-gas temperature distribution in Figure 10 clearly shows the redistribution of heat that takes place as the furnace goes from an unbalanced state to a balanced state. Thus, this case study clearly shows that a ROM with much lower computational requirements can successfully be used to balance a furnace through appropriate adjustments in fuel flow rates.

The run time of the control scheme, when deployed on the real-scale SMR, is expected to be a few hours (because of the computational overhead of the real-scale CFD model). Even after considering additional increments in the run time due to update iterations, the proposed scheme still offers distinct advantages, such as providing reliable quasi-real-time flow-adjustment recommendations and continuous monitoring

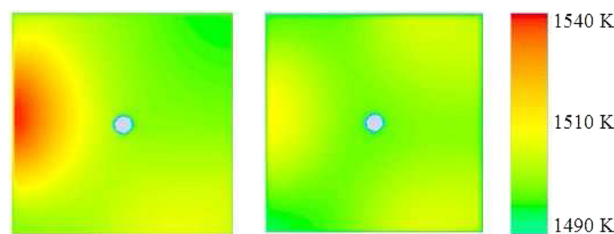


Figure 10. Color contours of the flue-gas temperature distribution at a height of 6 m for the unbalanced (left) and balanced (right) states. The balanced state was obtained through reduced-order-model (ROM)-based “furnace balancing”.

without manual interventions, over the heuristics-based adjustments, which are usually laborious and, therefore, performed infrequently. It is worth noting that large-scale systems such as SMR furnaces have characteristically slow dynamics (i.e., the furnace temperature field is not expected to change significantly during the time period over which the proposed control scheme executes). This allows the possibility of validating the recommended adjustments against CFD predictions before actual implementation.

CONCLUSIONS AND FUTURE WORK

In this paper, we addressed the issue of inefficient furnace operation in industrial steam-methane reformers (SMRs) and presented an algorithmic scheme for minimizing the temperature imbalance in the furnace. This is done by modulating the flow rate of fuel to the array of burners through integrated use of IR-based optical sensing, soft sensors, reduced-order modeling, and computational fluid dynamics (CFD). Through a simplified model, several practical aspects of “furnace balancing” were presented. Particularly, we explored the impact of fuel distribution on furnace temperature field, and their implications. We justified the need for incorporation of reduced-order modeling, and through a case study showed an initial validation of this strategy. Furthermore, we introduced a smart-manufacturing framework under which we advocated the deployment of our test-bed solution. In future work, we will report on the detailed application of unit-cell-based CFD modeling, along with the results from real-plant deployment of our proposed control scheme for furnace balancing.

ASSOCIATED CONTENT

Supporting Information

Tables S1 and S2 in the Supporting Information document segregates the equations solved outside and inside the tube. Brief explanations about the significance of various equations employed in the CFD model and enlisted in these tables have also been provided. In addition, parameter values and the boundary conditions employed in the CFD model corresponding to the output profiles shown in Figure 6 have been provided in Table S3. This material is available free of charge via the Internet at <http://pubs.acs.org/>.

AUTHOR INFORMATION

Corresponding Author

*E-mail: tfedgar@austin.utexas.edu.

Notes

The authors declare no competing financial interest.

ACKNOWLEDGMENTS

The authors gratefully acknowledge the financial support from the U.S. Department of Energy, through Grant No. DE-EE0005763/00011, "Industrial Scale Demonstration of Smart Manufacturing Achieving Transformational Energy Productivity Gains". MB was also partially supported by the Moncrief Grand Challenges Award from the Institute for Computational Engineering and Sciences at The University of Texas at Austin.

REFERENCES

- (1) Latham, D. A.; McAuley, K. B.; Peppley, B. A.; Raybold, T. M. Mathematical modeling of an industrial steam-methane reformer for on-line deployment. *Fuel Process. Technol.* **2011**, *92*, 1574–1586.
- (2) Slavejkov, A. G.; Li, X.; Joshi, M. L.; Waibel, R. T.; Bussman, W. LSV Burner Technology for Improved Efficiency, Reliability and Low-NO_x: A Case Study. In *Proceedings of the 51st Annual Safety in Ammonia Plants and Related Facilities Symposium*, Vancouver, Canada, Sept. 10–14, 2006.
- (3) McGreavy, C.; Newmann, M. W. Development of a mathematical model of a steam methane reformer. In *Proceedings of the Conference on the Industrial Applications of Dynamic Modelling*, Durham, NC, Sept. 16–18, 1969.
- (4) Zamaniyan, A.; Ebrahimi, H.; Mohammadzadeh, J. S. S. A unified model for top fired methane steam reformers using three-dimensional zonal analysis. *Chem. Eng. Process.* **2008**, *47*, 946–956.
- (5) Dunn, A. J.; Yustos, J.; Mujtaba, I. M. Modelling and Simulation of a Top-Fired Primary Steam Reformer using gPROMS. *Dev. Chem. Eng. Miner. Process.* **2008**, *10*, 77–87.
- (6) Olivieri, A.; Vegliò, F. Process simulation of natural gas steam reforming: Fuel distribution optimization in the furnace. *Fuel Process. Technol.* **2008**, *89*, 622–632.
- (7) Plehiers, P. M.; Froment, G. F. Coupled simulation of heat transfer and reaction in a steam reforming furnace. *Chem. Eng. Technol.* **1989**, *12*, 20–26.
- (8) Murthy, C. V. S.; Murthy, M. V. Modeling and Simulation of a Top-Fired Reformer. *Ind. Eng. Chem. Res.* **1988**, *27*, 1832–1840.
- (9) Singh, C. P. P.; Saraf, D. N. Simulation of Side Fired Steam-Hydrocarbon Reformers. *Ind. Eng. Chem. Process Des. Dev.* **1979**, *18*, 1–7.
- (10) Heynderickx, G. J.; Oprins, A. J. M.; Marin, G. B.; Dick, E. Three-dimensional flow patterns in cracking furnaces with long-flame burners. *AIChE J.* **2001**, *47*, 388–400.
- (11) Oprins, A. J. M.; Heynderickx, G. J.; Marin, G. B. Three-Dimensional Asymmetric Flow and Temperature Fields in Cracking Furnaces. *Ind. Eng. Chem. Res.* **2001**, *40*, 5087–5094.
- (12) Zheng, D.; Wu, B.; Fleitz, J.; Trajkovski, R.; Zhou, C. Q. CFD Simulation of a Hydrogen Reformer Furnace. In *Proceedings of the 14th International Heat Transfer Conference*, Washington, DC, Aug. 8–13, 2010; pp 233–244.
- (13) Davis, J.; Edgar, T.; Porter, J.; Bernaden, J.; Sarli, M. Smart manufacturing, manufacturing intelligence and demand-dynamic performance. *Comput. Chem. Eng.* **2012**, *47*, 145–156.
- (14) Korambath, P.; Wang, J.; Kumar, A.; Hochstein, L.; Schott, B.; Graybill, R.; Baldea, M.; Davis, J. Deploying Kepler Workflows as Services on a Cloud Infrastructure for Smart Manufacturing. *Procedia Comput. Sci.* **2014**, *29*, 2254–2259.
- (15) Oprins, A. J. M.; Heynderickx, G. J. Calculation of three-dimensional flow and pressure fields in cracking furnaces. *Chem. Eng. Sci.* **2003**, *58*, 4883–4893.
- (16) Stefanidis, G. D.; Merci, B.; Heynderickx, G. J.; Marin, G. B. CFD simulations of steam cracking furnaces using detailed combustion mechanisms. *Comput. Chem. Eng.* **2006**, *30*, 635–649.
- (17) Habibi, A.; Merci, B.; Heynderickx, G. J. Impact of radiation models in CFD simulations of steam cracking furnaces. *Comput. Chem. Eng.* **2007**, *31*, 1389–1406.
- (18) Ansys, Inc., <http://www.ansys.com/>.
- (19) ANSYS FLUENT Theory guide, Version 14.5; 2012.
- (20) Siegel, R.; Howell, J. R. *Thermal Radiation Heat Transfer*, 3rd ed.; Hemisphere Publishing Corporation: Washington, DC, 1992.
- (21) Kader, B. A. Temperature and concentration profiles in fully turbulent boundary layers. *Int. J. Heat Mass Transfer* **1981**, *24*, 1541–1544.
- (22) Xu, J.; Froment, G. F. Methane steam reforming, methanation and water-gas shift: I. Intrinsic kinetics. *AIChE J.* **1989**, *35*, 88–96.
- (23) Simpson, T. W.; Peplinski, J. D.; Koch, P. N.; Allen, J. K. Metamodels for Computer-based Engineering Design: Survey and recommendations. *Eng. Comput.* **2001**, *17*, 129–150.
- (24) Holmes, P.; Lumley, J. L.; Berkooz, G. *Turbulence, Coherent Structures, Dynamical Systems and Symmetry*, 1st ed.; Cambridge University Press: New York, 1998.
- (25) Krischer, K.; Rico-Martínez, R.; Kevrekidis, I. G.; Rotermund, H. H.; Ertl, G.; Hudson, J. L. Model identification of a spatiotemporally varying catalytic reaction. *AIChE J.* **1993**, *39*, 89–98.
- (26) Lang, Y.-d.; Malacina, A.; Biegler, L. T.; Munteanu, S.; Madsen, J. I.; Zitney, S. E. Reduced Order Model Based on Principal Component Analysis for Process Simulation and Optimization. *Energy Fuels* **2009**, *23*, 1695–1706.
- (27) Varshney, A.; Pitchaiah, S.; Armaou, A. Feedback Control of Dissipative PDE Systems using Adaptive Model Reduction. *AIChE J.* **2009**, *55*, 906–918.
- (28) Astrid, P.; Weiland, S.; Willcox, K.; Backx, T. Missing Point Estimation in Models Described by Proper Orthogonal Decomposition. *IEEE Trans. Autom. Control* **2008**, *53*, 2237–2251.
- (29) McKay, M. D.; Beckman, R. J.; Conover, W. J. A Comparison of Three Methods for Selecting Values of Input Variables in the Analysis of Output From a Computer Code. *Technometrics* **1979**, *21*, 239–245.
- (30) Dadebo, S.; Esposito, W. R. Production Control Utilizing Real Time Optimization. U.S. Patent No. 7,881,825. Feb. 1, 2011.